Experimental study of gravity currents moving over a sediment bed: suspension criterion and bed forms

Maria Rita Maggi, Maria-Eletta Negretti, Antoine Martin, Florence Naaim-Bouvet, Emil J Hopfinger

Experimental study of gravity currents moving over a sediment bed: suspension criterion and bed forms

Maria Rita Maggi[1*], Maria Eletta Negretti[1], Antoine Martin[1], Florence Naaim-Bouvet[2] and Emil J. Hopfinger[1]

[1]Univ. Grenoble Alpes, CNRS, Grenoble INP, LEGI, 38000, Grenoble, France.
[2]Univ. Grenoble Alpes, INRAE, UR ETNA, 38000, Grenoble, France.

*Corresponding author(s). E-mail(s): maria-rita.maggi@univ-grenoble-alpes.fr;
Contributing authors: maria-eletta.negretti@univ-grenoble-alpes.fr; antoine-martin@orange.fr ; florence.naaim@inrae.fr; emil.hopfinger@univ-grenoble-alpes.fr;

Abstract

In many natural settings, gravity currents flow over a mobile sediment bed as in fluvial outflows into lakes and reservoirs or in submarine canyons in coastal regions. We present experimental results which clarify the near-bed physical processes of sediment suspension, bed form development, as well as the effect of the erodible bed on the mean flow structure of the current. Compared with the flow over a fixed bed, the vertical velocity is directed downward above the mobile bed, indicating therefore slip with an increase in horizontal flux close to the sediment bed. The sediment suspension model developed here allows to determine the spatial evolution of sediment suspension up to maximum suspension capacity, in good agreement with experimental results of Garcia and Parker (1993)[1] as well as with the present sediment flux measured toward the downstream end of the sediment bed. Effects of local bursts, here intermittently caused by interfacial instability, tend to increase sediment suspension through increases in local shear velocity. Concerning bed forms, near bed scaling criteria suggest that in the present study the bed form consists of ripples

with the measured wave length being in agreement with criteria given by Lapotre et al. (2017)[2]. An expression for the ripple growth is given in relation with the theoretical criteria of Charru et al. (2013)[3].

Keywords: Gravity currents, Sediment Entrainment, Bedfoms

Article Highlights

- Experimental study of the gravity currents flowing over an erodible sediment bed and of the nature of the bed forms established by the current.
- The developed sediment suspension capacity model enables accurate prediction of the spatial evolution of sediment concentration in gravity currents up to saturation, corroborated by experimental data.
- The bed forms are characterized using hydrodynamic non-dimensional numbers, with their evolution and growth rates determined through a combination of experimental and theoretical analyses.

1 Introduction

Gravity currents are key processes that affect atmospheric [4], oceanic [5] and coastal circulations [6]. On a more local scale, these contribute to the shaping of the continental surface by landslides or snow avalanches [7, 8], and impact river outflows into lakes [9] and reservoirs [10]. In nature, the majority of gravity currents occur over complex terrains characterized by rough bottom or mobile sediment beds. Submarine currents are of particular importance in coastal regions since these currents have a large impact on the morphology of the seafloor and related ecosystems [6, 11–14]. Indeed, numerous submarine canyons sculpt the continental shelf, forming crucial conduits for the transport of shelf sediment to the deep ocean. Within these channels, sediments originate from either direct river input or the re-suspension of shelf sediment deposition facilitated by gravity flows.

The equilibrium of bed sediment transport depends on the inflow and the bed conditions such as momentum or buoyancy flux, turbulence intensity, bed shear stress and sediment bed properties. Bed shear and particle fall velocity are recognized as the most important parameters [15]. Sediment entrainment, suspension or deposition as well as bed forms have been mainly investigated in open channel flow conditions and in river flows [3, 16–20]. In gravity currents the coupling of hydrodynamics mechanisms and erosion, transport and deposition of sediments have mainly been investigated in the context of turbidity currents [21–25]. Entrained sediments in gravity currents can either be passively carried by the current or exert an influence on its dynamics by increasing the buoyancy flux, hence fueling a self-accelerating current [21, 26]. Powder snow avalanches are an example of such accelerating gravity current due to entrainment of sediment (snow) [8].

Understanding of sediment transport and bed forms related turbidity currents, as well as the impact of bed forms on velocity and density profiles, has been notably advanced by [27] various flow conditions and sediment types. Through experiments involving horizontal saline gravity currents over diverse sediment beds, [28] demonstrated a strong correlation between the bed and Reynolds shear stress in close proximity to the bottom, highlighting their significant role in sediment entrainment. Their findings revealed a feedback mechanism between the gravity current and the bottom sediments, influencing the hydrodynamics of the current itself. In experiments with salinity currents flowing down-slope over a mobile bed of different particle sizes, [1] determined the entrainment capacity using momentum and mass balance equations. Kyrousi et al. (2018)[29] performed Large Eddy simulations of lock-exchange gravity currents propagating over a mobile reach. They showed that, although shear stress is the main mechanism that sets particles into motion, turbulent bursts as well as vertical velocity fluctuations are also important to maintain sediments in suspension. In a gravity current, bursts may be triggered by shear instabilities at the interface as reported in [12, 30], who observed intermittently high values of bottom friction coefficients related with interfacial instability.

It is well known that the interaction between flow and erodible bed creates bed forms. Open channel flow laboratory experiments and field observations have allowed to establish the dependency of bedfoms on hydraulic conditions in terms of Froude number [3, 31, 32] or inner flow variables like the particle Reynolds number, Shields number, and Yalin number [2]. Despite the similarities between submarine gravity currents and open-channel flows in their capacity to shape bed forms, the hydraulic characteristics of gravity currents diverge from those of open-channel flows. Lapotre et al. (2017)[2] and Ohata et al. (2023)[33] demonstrated that the development of bed forms by saline-gravity currents can be compared with open-channel flow bed forms when scaled with inner variables, i.e. with dimensionless shear shear stress (Shields parameter) and particle characteristics.

The present experiments of saline gravity currents flowing over an erodible bed are complementary to the large data set obtained by [1]. Not considered by [1] are the changes in horizontal and vertical velocity profiles above the sediment bed. In comparison to the flow over a fixed bed, we show that the vertical velocity is directed downward above the mobile bed, indicating slip on the mobile bed, accompanied by an increase in horizontal flux in close proximity to the sediment bed. Furthermore, the sediment entrainment model developed here permits prediction of the downstream variations in sediment flux and sediment concentration above the bed. It demonstrates good agreement with both the experimental findings of [1] and the sediment flux measured at the end of the sediment bed in our current study. Concerning bed forms, we compare them with previous studies and use the analysis proposed by [2, 33] that allows to distinguish between ripples and dunes. Finally, we determine the ripple wavelength and amplitude and their variation in time. This analysis also suggests that the bed forms observed in the experiments of [1] are also ripples.

The paper is organized as follows: Sect. 2 provides essential details regarding the experimental apparatus and measurement techniques. The inner velocity flow and bed shear stress are discussed in Sect. 3. The sediment suspension capacity theory along with a comparison with the previous investigation by [1] is presented in Sect. 4. In Sect. 5, we delve into bed forms analyses, comparing them with previous studies [1–3, 33], with a specific focus on ripple evolution and growth rates. Finally, the conclusions are given in Sect. 6.

2 Experimental Setup and Procedure

The experiments, with a continuously supplied saline gravity current flowing over an erodible sediment bed, were conducted in a rectangular Perspex tank. A schematic representation of the experimental setup is provided in Fig. 1a. The initial section of the channel is horizontal, followed by a linear slope (θ=7°) that causes flow acceleration [30, 34]. The channel was initially filled with fresh and salty water (of densities ρ_a and ρ_1, respectively) to a height of $H_0 = 18 \pm 0.5\ cm$ from the bottom of the horizontal channel portion and separated by a gate located 160 cm upstream of the break in slope. At the beginning of the experiments the gate was opened to a height h_g with constant buoyancy supply assured by a pump. At the downstream end of the channel the flow was evacuated to prevent return currents and assure a constant total water depth H_0. The dense flow rate was set to $q_1 = 16\ \mathrm{cm}^2/\mathrm{s}$ per unit width. The overall Richardson number $Ri = 1/Fr_0^2$, with $Fr_0^2 = g_0' \delta_I / u_m^2$ at slope begin $x = 0$, is larger than 1, with $g_0' = \Delta\rho/\rho_a g = \sim 4.3 \pm 0.1\ cms^{-2}$ being the reduced gravity, $\Delta\rho = \rho_1 - \rho_a$ the density difference between the saline and the ambient quiescent water, δ_I the thickness of the velocity interface and u_m the maximum of the time averaged vertical velocity profile at $x = 0$. These initial conditions favor the sudden onset of shear instabilities after an initial downslope acceleration [34]. The initial Reynolds number is $Re = uh/\nu \approx 1500$.

The sediment bed starts at $x_{pb}/cos\theta$=10 cm downstream after the ridge and is 75 cm ($x_{sb}/cos\theta$) long and 4.5 cm deep (see Fig. 1a). The $x - z$ coordinate system represents the coordinate system relative to the inclined boundary with the origin at the ridge. The sediments used are polystyrene particles with a density of $\rho_s = 1040\ kg/m^3$, a particle settling velocity of $w_s = 1.3\ mms^{-1}$ [35], and a diameter $d_{50} = 300\ \mu m$. The particles were selected in order to ensure a suspension regime and avoid a wash load regime or a 100% bed load regime, considering the hydrodynamic conditions that could be easily achieved and maintained in the experimental channel [36]. These conditions correspond to a turbidity current composed of very fine suspension (fine silt) over a coarse sand bottom [6]. Particle size distributions of the sediments were analyzed with a Spraytec laser particle size analyzer (Fig. 1b). Their particle Reynolds number is $Re_p = \sqrt{g_s' d_{50}} d_{50}/\nu = 2.7$ with $\nu = 1.14 \times 10^{-6}\ m^2 s^{-1}$ and the reduced gravity $g_s' = g(\rho_s - \rho_1)/\rho_1 = 0.34\ ms^{-2}$, where ρ_s is the sediment density. The dimensionless grain size is $d^* = \left[\frac{g_s' d_{50}^3}{\nu^2}\right]^{1/3} = 1.9$. For small enough

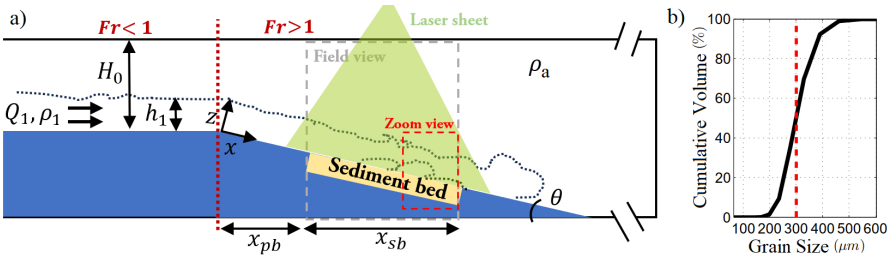

Fig. 1: a) Sketch of the experimental setup (not scaled). Q_1 is the pump flow rate, $Fr = g_0' h_m / u_m^2$ is the densimetric Froude number, ρ_a and ρ_1 denote the densities of the ambient fluid and the gravity current, respectively. The depth of the dense current upstream of the slope is $h_1 = 4$ cm, $x_{pb}/cos\theta = 10$ cm is the distance between the ridge and the initiation of the sediment bed, and $x_{sb}/cos\theta = 75$ cm is the length of the sediment bed. b) Grain-size distribution of the sediment bed (black curve) and median grain size diameter $d_{50} = 300\ \mu m$ (dashed vertical red line).

d_{50} as in our case, the bottom layer corresponds to the viscous sublayer, with a thickness that is approximately six times the viscous length $\delta_\nu = \nu/u_*$. The flow is said to be dynamically smooth on the particle size, but rough on the bed form size.

Particle Image Velocimetry (PIV) was employed to measure the instantaneous velocity field. Orgasol particles with a mean diameter of 30 μm were added in both salt and fresh water as seeding material. A 6W argon-ion laser (Coherent), operating in multimode, was used as a continuous light source. The generated laser sheet spans a length of approximately 1 m and a width of 5 mm and was positioned in the middle of the sediment bed area. The field of view covered the entire sediment bed area, with an additional zoomed view (9.5×11.3 cm) at the final portion of the sediment bed. 8000 to 12000 images were taken with a CCD camera (1200 x 1600 pixels) at a frequency of 22.5 Hz resulting in a spatial resolution of 0.23 cm x 0.23 cm for the larger field of view and of 0.1 cm x 0.1 cm for the zoomed view. The experiment was repeated 3 times. The experiment on sediment bed (SB) has been compared to an experiment over a smooth bed (NS) with the same initial conditions. The main parameters of the experiments, along with those from [1], are presented in Table 1.

3 Velocity fields and bed shear stress

Velocity fields of both runs SB and NB were analyzed and compared at three distinct positions downstream of the ridge: $x = 5h_1$ (1), $x = 15h_1$ (2), and $x = 18.5h_1$ (3), with h_1 the depth of the current at the ridge (Fig. 2a).

Fig. 2 shows time averaged vertical profiles of the streamwise and vertical velocity components $\langle u \rangle$ and $\langle w \rangle$, respectively, obtained neglecting the data

Table 1: Characteristic parameters of the experiments conducted with sediment bed (SB) and for the study of [1] (Run B3 and C1). U and h are the vertical averaged velocity and depth of the dense flow, respectively. $Fr_0 = U/(g_0' h)^{1/2}$ is the Froude number with $g_0' = \Delta\rho/\rho_a g$ being the reduced gravity and $Re_0 = (Uh)/\nu$ is the Reynolds number of the flow. d_{50} is the mean diameter of the sediment particles, w_s is the particle settling velocity and ρ_s is the sediment density. $Re_p = \sqrt{g_s' d_{50}} d_{50}/\nu$ denotes the particle Reynolds number where $g_s' = g(\rho_s - \rho_1)/\rho_1$ is the reduced gravity. E_S is the sediment entrainment rate, E_s^* is the sediment entrainment coefficient, u_* is the shear velocity in the presence of bed forms and u_{*s} the effective averaged shear velocity (skin friction) on the erodible bed. $Re_* = (u_{*s} d_{50})/\nu$ is the shear Reynolds number and $\tau_{*s} = (u_{*s}^2)/(g_s' d_{50})$ is the bed shear stress due to skin friction.

Run	$x_1 - x_2$ (cm)	U (cm/s)	h (cm)	Fr_0	Re_0	d_{50} (cm)
SB	$55 - 60$	5.2	3.7	1.3	1900	0.03
B3	$200 - 400$	10.2	5.0	1.0	3400	0.018
C1	$350 - 400$	8.0	6.1	0.7	3200	0.018

Run	w_s (cm/s)	ρ_s (kg/m^3)	Re_p	E_s ($\cdot 10^{-3}$)	E_s^* ($\cdot 10^{-3}$)	u_* (cm/s)	u_{*s} (cm/s)	Re_*	τ_{*s}
SB	0.13	1040	2.7	7.9	2.86	0.9	0.6	1.58	0.35
B3	0.42	1350	2.9	1.3	1.1	2.0	1.2	1.44	0.15
C1	0.42	1350	2.9	4.3	3.4	2.39	1.25	1.50	0.16

of the initial passage of the current head. The experiment SB can be subdivided in two phases, the first one with developing bed forms, and the second one characterized by the fully developed bed forms, which alter the velocity field, the bed shear stress and the sediment concentration. The so chosen time intervals for time average are $70 < t < 150$ s and $t > 150$ s. While for the streamwise component $\langle u \rangle$ no significant differences between the two cases SB and NS are reported (see Fig. 2(b,c,d)), the behaviour of the vertical velocity component $\langle w \rangle$ is very different.

At the top of the slope at $x = 5h_1$, Fig. 2e displays negative values in both experimental runs NB and SB, but attributable to the acceleration of the dense flow, with larger values for the SB run. When moving further downstream, at $x = 15h_1$ and $18.5h_1$, the SB run still exhibits high negative values of $\langle w \rangle$ in the inner part of the current. In contrast, in the NS run, the negative values are only observed in the outer part of the dense current due to interfacial entrainment (Fig.2(f,g)). These negative values of $\langle w \rangle$ in the SB run indicate slip on the mobile bed with an increase in horizontal flux close to the sediment bed.

Fig.3 displays the time averaged Reynolds shear stresses $\langle u'w' \rangle$ at the chosen positions $x = 5h_1$, $x = 15h_1$, and $x = 18.5h_1$, where u' and w' are respectively the time fluctuation of the two velocity components such as $u' = u - \langle u \rangle$ and $w' = w - \langle w \rangle$. At $x = 5h_1$, Reynolds stresses are negligible

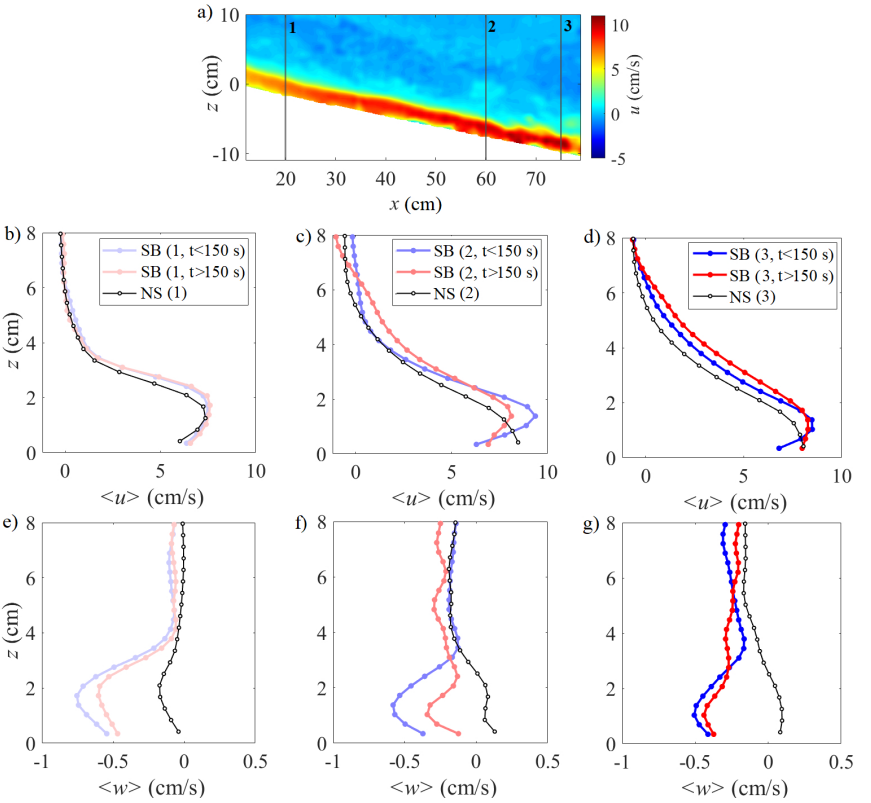

Fig. 2: a) Instantaneous along-slope velocity field. Velocity profiles were computed at the three vertical sections. Vertical profiles of the mean streamwise velocity $\langle u \rangle$ (b, c, d) and the normal velocity component $\langle w \rangle$ (e, f, g) obtained at three different locations along the slope ($1 : x = 5h_1$, $2 : x = 15h_1$, and $3 : x = 18.5h_1$) for SB (sediment bed) and NS (smooth bed) runs. Temporal averages were calculated over the following time intervals: $t = 70 - 150$ s and $t > 150$ s for the SB run.

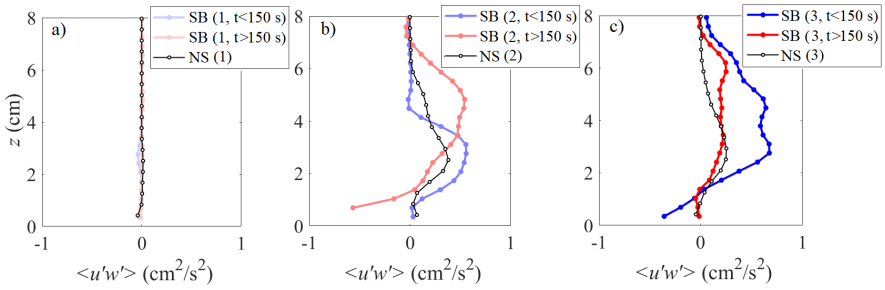

Fig. 3: Vertical profile of the Reynolds shear stress $\langle u'w' \rangle$ at $1 : x = 5h_1$, $2 : x = 15h_1$, and $3 : x = 18.5h_1$ for the SB and NS runs. Temporal averages were calculated over $t = 70 - 150$ s and $t > 150$ s for the SB run.

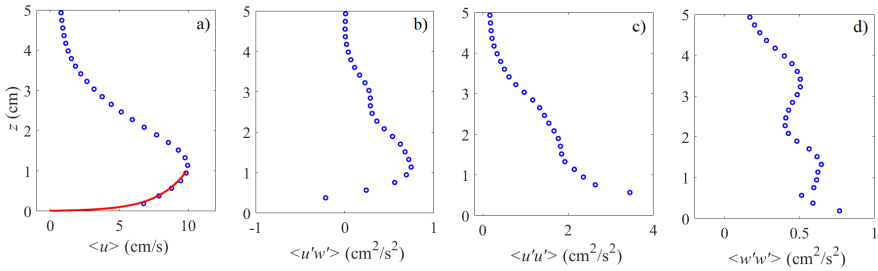

Fig. 4: Vertical profiles of (a) the time averaged streamwise velocity $\langle u \rangle$, (b) the Reynolds shear stress $\langle u'w' \rangle$ and (c) the normal Reynolds stress $\langle u'u' \rangle$ and (d) $\langle w'w' \rangle$ obtained from the zoomed view at $x = 15h_1$. The red curve in (a) represents the streamwise velocity modeled with the logarithmic law at the wall to evaluate u_*.

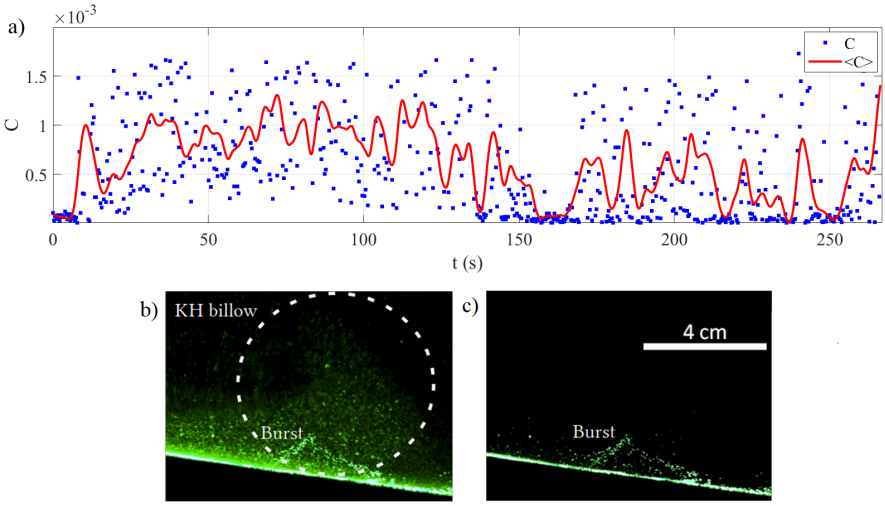

Fig. 5: a) Instantaneous (blue dots) and fitted (red line) concentration of sediment particles overtime at the downstream end of the erodible-bed. b) Instantaneous image showing a raw image with a Kelvin-Helmholtz (KH) billow in development connected with boundary layer separation and bursts of sediment suspension, with the corresponding filtered image to quantify the suspension (c).

in all runs (Fig.3a) and differences appear further downstream. At $x = 15h_1$, $18.5h_1$, the SB run values are larger than in the NS run concentrated in the sheared interface (Fig. 3b). These are shifted further above spread throughout the entire current depth for $t > 150$ (red lines).

The intensity of shear stress within the lower boundary layer governs the sediment transport capacity of saline currents, influencing whether erosion or

deposition processes dominate at the bottom boundary. The bed shear stress (τ_b) is not directly measured but rather deduced from assessments of the friction velocity (u_*). Several approaches exist for evaluating friction velocity [1, 33, 37]. Unfortunately, the near-boundary region poses the largest challenge for obtaining trustworthy velocity measurements, given that it is the location with the higher velocity gradients. Assuming a flow that gradually varies in the longitudinal direction, that is essentially two-dimensional in the vertical plane, the streamwise velocity can be modeled by the logarithmic law of the wall (e.g. [27, 38]):

$$u(z) = \frac{u_*}{\kappa} ln\left(\frac{z}{z_0}\right) \tag{1}$$

where u_* is the friction velocity, $\kappa = 0.405$ is the von Kármán constant [27], and z_0 is the zero-velocity level. While a good confidence in the estimation of u_* is reachable, the estimation of z_0 is very sensitive to the knowledge we have of the true bottom level [27]. A sensitivity analysis of the choice of z_0 varying of 50% gives variations of the shear velocity u_* of 8% maximum.

An estimation of the friction velocity u_* can be obtained from Eq. (1), for which the data of the zoomed view with higher spatial resolution at $x = 15h_1$ has been used; the so computed value is $u_* = 0.9\ cms^{-1}$ (Fig.4a). Using the same procedure, we obtain $u_* = 0.65\ cm\ s^{-1}$ for the NS run. To obtain an accurate measure of boundary shear velocity, it is necessary to consider the resistance encountered by an underflow moving over an erodible bed covered with bed forms [1]. The total friction velocity u_* can be seen as the combination of two contributions: the skin friction u_{*s} and the form drag u_{*f}. Consequently on a sediment bed the skin friction velocity is likely to be slightly less, i.e. $u_{*s} \simeq 0.6\ cm/s$. The values of u_* and of u_{*s} are listed in Table 1 together with those of Garcia and Parker (1993)[1]. Fig. 4(b,c,d) displays the averaged Reynolds stresses $\langle u'w' \rangle$, $\langle u'u' \rangle$ and $\langle w'w' \rangle$, respectively from the zoomed view. The vertical profiles of $\langle w'w' \rangle$ and $\langle u'u' \rangle$ appear different from those of a turbulent wall jet [39]. Near the wall $\langle w' \rangle = \mathcal{O}(u_*)$.

4 Sediment Suspension and Transport Capacity

An estimation of the particle concentration C over time is depicted in Fig. 5, giving a $\mathcal{O}(10^{-3})$ (see the appendix A for the detailed computation procedure). In this figure we see that the averaged value decreases after the formation of bed forms ($t = 150$ s, see also section 5 further below). Peak values can be attributed to bursts consisting in intermittent ejections of sediments from the bottom coupled with the development of interfacial instabilities [34]. An instantaneous snapshot of this phenomenon is given in Fig. 5b with the corresponding filtered image that highlights the sediment suspension in Fig. 5c.

4.1 Sediment Suspension Capacity

The change in sediment flux ($CUh \equiv \int_{z_b}^{\infty} u(z)c(z)\,\mathrm{d}z$) of a dense bottom current flowing over an erodible sediment bed can be written as:

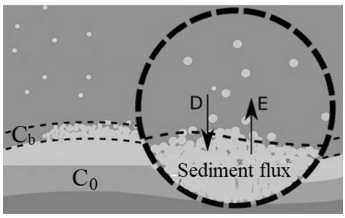

Fig. 6: Sketch of the sediment flux dynamics. E is entrainment of sediment from the sediment layer, D is the deposition, C_b is the near-bed sediment concentration, and C_0 is the concentration of the sediment layer.

$$\frac{dCUh}{dx} = E - D \tag{2}$$

where C is the volume sediment concentration, E is entrainment of sediment from the erodible sediment layer and D is deposit. It is generally accepted [1, 17] that $D = C_b w_s$, where C_b is a near bed sediment concentration (cf. sketch in Fig. 6), taken at $0.05h$ [1] and w_s is the particle settling velocity. Concerning E, there is less consensus. Celik and Rodi (1991)[17] take $E = w_s C_{bmax}$ with C_{bmax} the maximum near bed concentration the flow can carry, which is similar to $E = w_s E_S$ used by [1]. Hence:

$$\frac{dCUh}{dx} = w_s(E_S - C_b). \tag{3}$$

From Eq. (3) an expression for the spatial change in near bed concentration C_b can be obtained assuming that the mean concentration C in the current is a fraction of C_b. Specifically $C = \beta C_b$, where $\beta \approx 0.5$ in accordance with the measurements of [1] that $C_{bmax} \approx 2C_{max}$, we can write Eq. (3) in the form:

$$\frac{Uh}{2w_s}\frac{dC_b}{dx} + \frac{EU}{2w_s}C_b + C_b = E_S, \tag{4}$$

with the ambient fluid entrainment coefficient $E \approx 0.01$ [40]. The equation governing the spatial change in sediment concentration reads:

$$\frac{dC_b}{dx} + aC_b - B = 0 \tag{5}$$

where the values of the factor a:

$$a = (2w_s + EU)/(Uh) = 1/L_S \tag{6}$$

can be determined from the parameters given in Table 1, with L_S being a saturation length which will be discussed further below. The general solution of Eq. (4) is:

$$C_b = -Ae^{-ax} + B. \tag{7}$$

When $x \to \infty$, $C_b = C_{bmax} = E_S$, entrainment is equal to deposition (Eq. 4), hence, $B = E_S$ and when $x = x_0$, $C_b = 0$, hence $A = E_S$. The distance x_0 at which sediment entrainment and deposition begins is taken as U times the overturning time of eddies of size δ, i.e. $x_0 \approx (\pi\delta/(u' - w_s))U$. This gives for the experiments of [1], about 30 to 60 cm, depending on the value of δ chosen; the experiments of [1] suggest $x_0 \approx 40$. For the present study we take $x_0 \approx 30$ because $(U/u' - w_s)$ and δ are slightly less. In any case, the distance x_0 has to be larger than the first bed form length, which is about 25 cm. The expression is thus:

$$C_b = E_S \left(1 - \exp^{-(x_s - x_0)/L_S}\right), \tag{8}$$

with x_s starting on the sediment layer.

4.2 Determination of bed sediment entrainment E_S

Sediment entrainment depends on the shear stress:

$$w_s E_S = \overline{w'c'}|_{z_0} = u_{*s} C_0 E_s^* \tag{9}$$

where C_0 is the concentration of the sediment layer, usually equal to 0.6 [3] (may be less when ripples or dunes are formed) and E_s^* is an entrainment coefficient. Considering Eq. (9), Eq. (3) then takes the form:

$$\frac{dCUh}{dx} = w_s \left(C_0 \frac{u_{*s}}{w_s} E_s^* - C_b\right). \tag{10}$$

It may be noted that w_s should be replaced by $w_s cos\theta$ which, for 7°, is a negligible correction and thus is ignored. In gravity currents, sediment entrainment increases the buoyancy flux with the total flux given by [1] $\Phi(x) = \Phi_0 + g'_s q_s$, where Φ_0 is the buoyancy flux of the saline current and $q_s = CUh$. In the present experiments the ratio $g'_s q_s/\Phi_0 \ll 1$, i.e. the buoyancy flux is not affected by the entrained sediment (negligible current acceleration). Note also, that the energy drain by the suspended sediment $\partial E_p/\partial t = g'_s C_{max} w_s$ has to be negligible compared with turbulent kinetic energy (TKE) production by shear.

The Shields parameter of $\tau_0/(\rho_s - \rho)gd$ vs. $Re_* = u_* d/\nu$ gives the limit of sediment movement. For sediment suspension, the shear stress must be higher than the Shields limit and Celik and Rodi [17] propose for open channel flows on a sediment bed the criteria:

$$\tau_{*s} = \frac{\rho u_{*s}^2}{(\rho_s - \rho)gd} = \begin{cases} 0.15/Re_* \text{ when } \mathrm{Re}_* \leq 0.6 \\ 0.23 \text{ when } \mathrm{Re}_* \geq 0.6 \end{cases} \tag{11}$$

which is likely to be generally valid.

In order to predict the spatial evolution of the bed sediment concentration C_b up to saturation we have to define the bed sediment entrainment E_S. Garcia

and Parker [1] give an expression for E_S in the form:

$$E_S = \frac{AZ_u^5}{(1 + \frac{A}{0.3}Z_u^5)} \tag{12}$$

where $A = 1.3 \cdot 10^{-7}$, $Z_u = u_{*s}/w_s f(Re_p)$ and $Re_p = (g'_s d_{50})^{1/2} d_{50}/\nu$. The function $f(Re_p) = 0.586 Re_p^{1.23}$ is fitted to the measured values of E_S. For small values of Z_u, $E_S = AZ_u^5$ and for large values, such that $(Z_u^5 A/0.3) \gg 1$, $E_S = 0.3$. In the present experiments $Re_p = 2.7$ so we get $E_S \approx 8 \cdot 10^{-3}$. The saturation value of $E_S = 0.3$ would be reached when $(Z_u^5 A/0.3) \approx 10$, i.e. when $u_{*s}/w_s \geq 15$.

Celik and Rodi (1991)[17] derived a transport capacity correlation for C_{max} in the form $C_{max} = 0.034F$, i.e.:

$$C_{max} = 0.034 \frac{u_{*s}^2}{g'_s h} \frac{U}{w_s}. \tag{13}$$

In the present experiment $U \approx 8.5 u_{*s}$, hence, C_{max} is given by:

$$C_{max} \simeq 0.29 \frac{u_{*s}^2}{g'_s h} \frac{u_{*s}}{w_s} \simeq \frac{E_s^*}{2} \frac{u_{*s} C_0}{w_s}. \tag{14}$$

With $C_{bmax} \simeq 2C_{max}$, $E_s^* = u_{*s}^2/(g'_s h) \simeq 2.86 \cdot 10^{-3}$, and from Eq. (9) $E_S = 7.9 \cdot 10^{-3}$. This value is very close to that obtained from the relation given by [1], but the saturation value of 0.3 is not realistic for large u_{*s}/w_s. The relation of [17] indeed shows that even for u_{*s}/w_s of order 10^2, the maximum mean concentration is of order 10^{-2} (their Fig. 1).

Fig. 7 shows C_b/C_{bmax} vs $(x_s - x_0)/L_S$ for experiments B3 and C1 of [1] as well as for the present experiment. The continuous line represents Eq. (8) ($C_{bmax} = E_S$). There is good agreement between theory and experiments considering the uncertainty in the measurement of near bed sediment concentration.

For C_{bmax} to be reached, the sediment bed has to be long enough, i.e. about three times L_S (see Fig. 7), which is not the case in the present experiment. As seen in Fig. 5, there are intermittent bursts that are correlated with the KH instability at the interface and these bursts cause sediment ejection.

5 Definition and evolution of the bed forms

An important result of the current experiments is the development of bed forms which, although widely reported in the literature (e.g. [1, 33, 41–43]), are still intriguing. While most observed bed forms are discussed in relation to open channel flow above a sediment bed, gravity current hydrodynamics are dependent on vertical density variation, and therefore are fundamentally different from open-channel flows. Consequently, despite decades of observations of bed forms, there is a lack of a universal scaling relation to predict

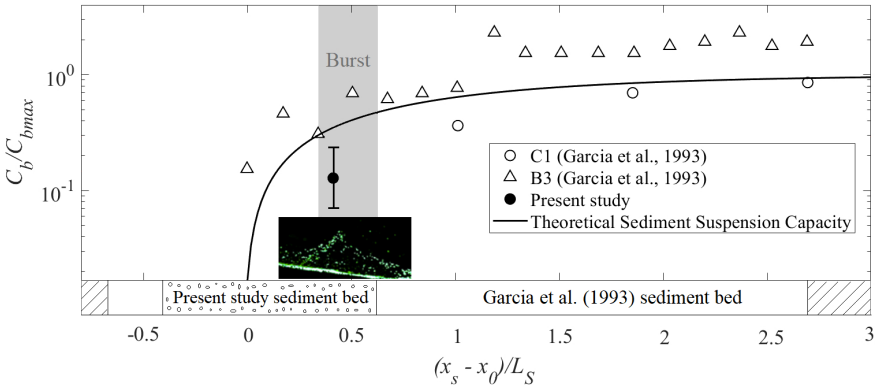

Fig. 7: Non-dimensional spatial relaxation of the ratio between the near-bed concentration C_b and the maximum near-bed concentration C_{bmax}. Empty symbols: [1], filled symbol: present experiment. C_{bmax} is $1.3{\cdot}10^{-3}$ and $4.2{\cdot}10^{-3}$ for [1] and for the present study is $7.9{\cdot}10^{-3}$. The saturation length L_S is ≈ 0.6 m and ≈ 0.7 m, respectively. The solid black line represents the theoretical sediment concentration Eq.(8) with $L_S = 0.6$m.

their classification (dunes and ripples), their characteristic length scales and their growth rate. Ripples have generally a lower amplitude-wavelength ratio Δ/λ. Sequeiros et al.(2010)[27] even classifies as a plane bed those experiments forming ripples with $\Delta = \mathcal{O}(mm)$. Garcia and Parker (1993)[1] observes well-defined ripples interpreted as downstream-migrating antidunes.

Few recent studies attempt to classify bed forms in gravity current deposits as a function of the relevant hydrodinamic non-dimensional numbers as the particle Reynolds number and the Shields stress, combination of which is the so called Yalin number $\chi = Re_*\sqrt{\tau_*}$ [2, 3, 33].

5.1 Equilibrium bed forms

It is of interest to characterize the equilibrium bed forms in the present experiments in terms of the analysis of Lapotre et al. (2017)[2] and the saline-gravity currents analysis of [33] and their development in the light of the theoretical concepts in [3]. In Fig. 8a the Hovmöller diagram of the bed elevation anomaly shows that periodic bed forms appear and grow in time until reaching an equilibrium at the end of the experiment: from $t > 150$s, bed forms appear to be stationary. This is corroborated in Fig. 8b showing the Hovmöller diagram of the bed elevation anomaly spatial correlation function by which we compute an average wavelength $\lambda = 9.0 \pm 1$ cm and an amplitude $\Delta_{max} \simeq 2.5 \pm 1$ mm (Fig. 8a) at the end of the experiment.

Lapotre et al. (2017)[2] used a large dataset of open channel flow to predict the formation of ripples, and found that ripples form for Yalin numbers, χ, below a certain threshold. Below that threshold, they showed that the dimensionless wavelength of the smaller bed forms, λ^*, collapses to a single power-law

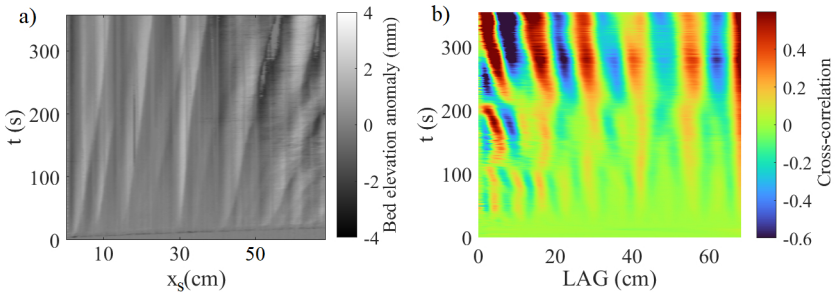

Fig. 8: Hovmöller diagram of the bed elevation anomaly (a) and of the spatial auto-correlation function of the bed elevation anomaly (b).

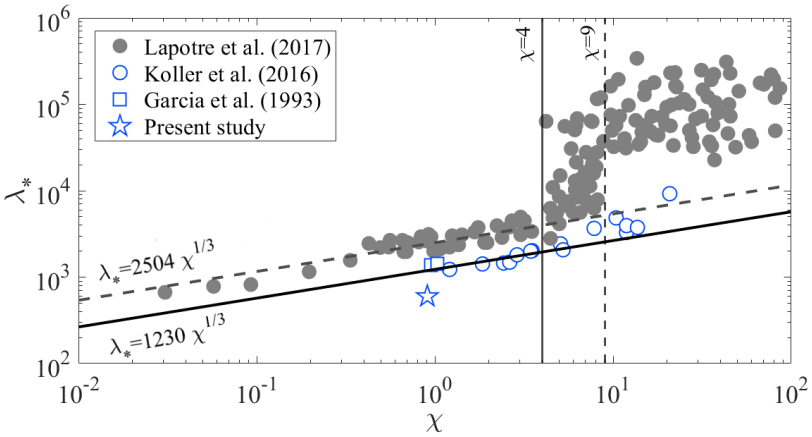

Fig. 9: Dimensionless wavelength $\lambda_* = \lambda u_{*s}/\nu$ vs the Yalin number $\chi = Re_*\sqrt{\tau_{*s}}$ using the scaling relation proposed by [2, 33, 44]. Grey symbols represent the open-channel flows data from [2], while blue symbols represent the gravity currents data: square symbols [1], round symbols [18], and star symbol for the present study. Vertical lines define the ripples ($\chi < 4$), transitional bed forms ($4 < \chi < 9$), and dunes ($\chi > 9$) areas, respectively as identified by [2] for open-channel flow cases. The dashed line represents the fit of the results from [2] ($\lambda_* = 2504\chi^{1/3}$), while the solid line represents the fit of the experiments with density currents, i.e., [1, 18], and our study ($\lambda_* = 1230\chi^{1/3}$).

relation:

$$\lambda_* = 2504\chi^{1/3} \tag{15}$$

where $\lambda_* = (\lambda u_{*s})/\nu$ is the non-dimensional wavelength of the bed form.

Lapotre et al.(2017)[2] (see also [33]) classify bed forms as ripples for $\chi < 4$ with the most probable wavelength of $\lambda = 12$ cm for siliciclastic grains in freshwater, which is in agreement with our observation ($\lambda = 9.0 \pm 1$). In Fig. 9 we report the data of [2] and add the data of saline gravity currents of

[1, 18] and our experiment. The saline gravity current data of the present study and those of [1], although not entirely in agreement results with Lapotre et al.(2017)'s [2], fall within the ripple area ($\chi < 4$) and are consistent with some of the data from [18] for saline-gravity currents.

The value of λ_* in the present experiments and those of [1, 18] is somewhat smaller than the one obtained with Eq. (15) (see also [33]). Using our values for $Re_* = (u_{*s}d_{50})/\nu = 1.58$ and $\tau_{*s} = 0.35$ we obtain $\chi \approx 0.94$ and $\lambda_* \approx 530$ which is smaller than λ_* obtained following Eq. (15), corresponding to a wavelength of $\lambda \approx 47$ cm.

Eq. (15), derived by [2], serves as prediction of ripple size in open-channel flows. This equation makes use of the Yalin number, which, in the context of bedload sediment transport, is proportional to the sediment saturation length. For gravity currents dominated by suspended sediment transport, the dimensionless ripple wavelength λ_* is also expected to be proportional to $(L_S u_*/\nu)^{1/3}$, where L_S represents the saturation length for suspension rather than bedload (see also [27]). Consequently, it is unsurprising that gravity-current bed form data follows a power-law with a similar exponent but is offset compared to open-channel ripples.

The saline-gravity currents data are better fitted by the relation:

$$\lambda_* = 1230\chi^{1/3}, \tag{16}$$

which is represented by a solid line in Fig. 9.

Lapotre et al. (2017) [2] and Duran et al. (2019) [44] identified the ripple-to-dune transition in open-channel flows to likely occur for $\lambda_* \approx 4000$, which corresponds to a value of $\chi = 4$ using the relation (15). Using our relation Eq. (16) with $\lambda_* \approx 4000$, gives the transition ripple-to-dune for $\chi \approx 35$ in saline gravity currents. This suggests, in accord with the experimental data reported in Fig. 9, that the ripple-to-dune transition for gravity currents may occur at larger Yalin numbers χ as compared to open channel flows. However, further experimental tests are necessary to accurately define the ripple-to-dune transition for gravity flows and better understand its dynamics.

Focusing on the size of the bed forms, our λ value is comparable to that reported by Garcia and Parker (1993) [1], ranging between 10 and 16 cm, while the amplitude Δ is one order of magnitude lower. The bed forms identified by Garcia and Parker (1993)[1] also fall perfectly within the definition area of ripples and are in perfect agreement with the previous study of Koller et al. (2016)[18]. Bed forms were classified also using a Shields diagram in the Re_* and τ_{*s} parameter space, recently revisited by Lapotre et al. (2017)[2], who includes the threshold values $\chi < 4$ and $\chi > 9$ for the formation of ripples and dunes, respectively. This is given in Fig. 10 where we also incorporate non-dimensional wavelengths of the bed form, λ_*, defined by the power-law Eq. (16) (solid lines). It is noteworthy that the data of [1] (squares) and of the present study (star) fall within an interval of $\lambda_* \approx 1250$. This result overestimates our average value of λ, but perfectly matches that of [1] ($\lambda \approx 12$ cm).

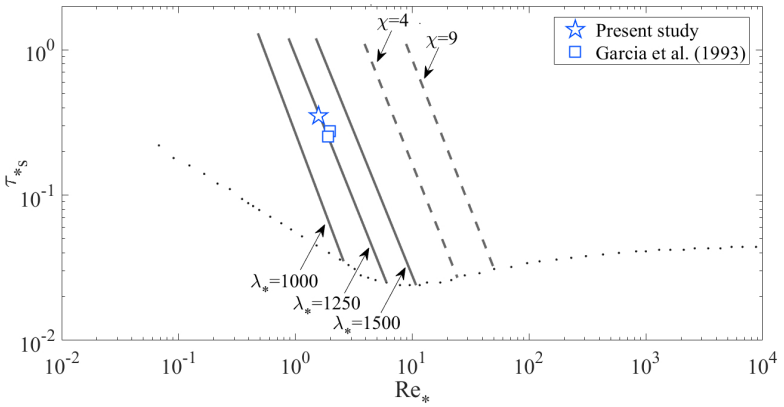

Fig. 10: Dimensionless Shields stress τ_{*s} vs shear Reynolds number $Re_* = u_{*s}d_{50}/\nu$, incorporating non-dimensional wavelengths of the bed form, λ_*, defined by our new power-law Eq. (16) (solid lines) and Yalin numbers χ (dashed lines) defined by [2] for the open-channel flows. The square symbols represent the experiments of [1], while the star symbol represents present experimental result.

5.2 Temporal development of bed form

To define the ripple evolution and ripple growth rates, we illustrate in Fig. 11 the evolution of our sediment bed over time. Herein, we highlight the time for transition for the steady bed forms $t = 150$ s. Fig. 11a illustrates the spatial evolution of the sediment bed over time and distinctly highlights two trends: one for $x_s < 40$ cm and another for $x_s > 40$ cm. Specifically, for $x_s < 40$ cm, the positions of the ripples seem to remain stable with a slightly increasing wavelength over time. However, in the region characterized by shear instabilities ($x_s > 40$ cm), the shapes of the bed forms become notably more complex. This behavior is further confirmed in Fig. 11b, where the temporal evolution of the averaged wavelength λ is reported. The white markers correspond to the total spatial average λ, while the grey circles represent the spatial average for $x_s > 40$ cm over time, exhibiting values fluctuating between 5 and 14 cm for $t > 150$ s.

Fig. 11c depicts the longitudinal bed profiles at different times in the measured domain. It is observed that the amplitude of the ripples generally increases over time. However, after $t = 150$ s for $x_s < 40$ cm, the change in Δ is smaller compared to locations further downstream. The average growth of Δ is shown in Fig. 11d, revealing a fast increase at the beginning and which slows down from $t > 50$s. The growth of a ripple crest up to saturation is of the form:

$$\Delta = \Delta_{max}\left(1 - \exp^{-t/T_S}\right) \tag{17}$$

where the growth rate $\sigma = 1/T_S$ can be determined by fitting Eq. (17) to the experimental data. It is of interest to compare this σ with the value given

in Charru et al. (2013)[3] that is of the form $\sigma = B(kz_0)Qk^2$, where $B = 1.06(k\delta_v)^{-2/3}sin(\pi/6)$ and Q is:

$$Q = \frac{\tau_s}{0.6}\frac{\partial q_{sat}}{\partial \tau_s}\bigg|_{\tau_s}. \tag{18}$$

From Eq. (18) we get $Q \simeq 5.6 \cdot 10^{-2} cm^2 s^{-1}$ (noting that $q_{sat} \equiv q_{max} = C_{max}hU$) and with $\delta_v = \nu/u_{*s}$, and $k = 2\pi/\lambda = 0.78$ (taking $\lambda \simeq 8cm$ at $t = 150s$) we get $T_S = 1/\sigma \simeq 144s$. As is seen in Fig. 11d, with this value of T_S, Eq. (17) is in good agreement with the experiment. The expression of bed form growth rate given by $\sigma = B(kz_0)Qk^2$ [3] has been obtained from linear stability analysis of the sediment mass conservation equation and would thus be valid only in the linear regime. However, Eq. (17) contains q_{sat}, i.e. the bed form growth up to saturation. According to [3], the ripple phase velocity $c = \omega/k$ is expressed by

$$c = A(kz_0)Qk, \tag{19}$$

where $A = 1.06(k\delta_v)^{-2/3}cos(\pi/6)$ and is ≈ 15 in the present experiments. This gives, according to Eq. (19), $c \approx 0.6$ cm/s that is one order of magnitude larger than the experimental value $c_{exp} \approx 0.02$ cm/s.

Furthermore, it is interesting to note the existence of a relation between L_S and T_S which can be established from the mass conservation equation:

$$\frac{\partial C_0 h_s}{\partial t} = -\frac{\partial q}{\partial x} \tag{20}$$

where h_s is the bed layer thickness with bed sediment concentration $C_0 = 0.6$. The change of bed layer thickness is related with the change in bed form amplitude: $C_0 \partial h_s/\partial t = -\alpha \partial \Delta/\partial t$ [19]. Hence, from Eq. (8) and Eq. (17) we get:

$$\alpha \frac{\Delta_{max}}{T_S} \exp^{-t/T_S} = \frac{q_{max}}{L_S} \exp^{-(x_s - x_0)/L_S}. \tag{21}$$

When $t = T_S$ and $(x_s - x_0) = L_S$, $\alpha \Delta_{max} = q_{max} T_S/L_S$. In accordance with Fig. 11d with $q_{max} = C_{max}hU = 6.6 \cdot 10^{-2} cm^2/s$, $T_S = 150$s and $L_S = 60$ cm, we compute $\Delta_{max} \simeq 1.7$ mm which is in very good agreement with the observed value of Δ at $t = T_S$ with $\alpha \approx 1$. The measured change in bed layer thickness is $\delta h_s \simeq 2.5$ mm corresponding to the value obtained from Eq. (20).

6 Further Discussions and Conclusion

The present study regarding gravity currents flowing over an erodible sediment bed clarifies the physical processes of sediment suspension capacity, as well as the nature of the bed forms established by the current. The primary goal of the study is to develop a sediment suspension capacity model that enables accurate prediction of the spatial evolution of sediment concentration in gravity currents up to saturation, corroborated by experimental data. To clarify the near-bed physical processes of gravity currents flowing over sediment beds,

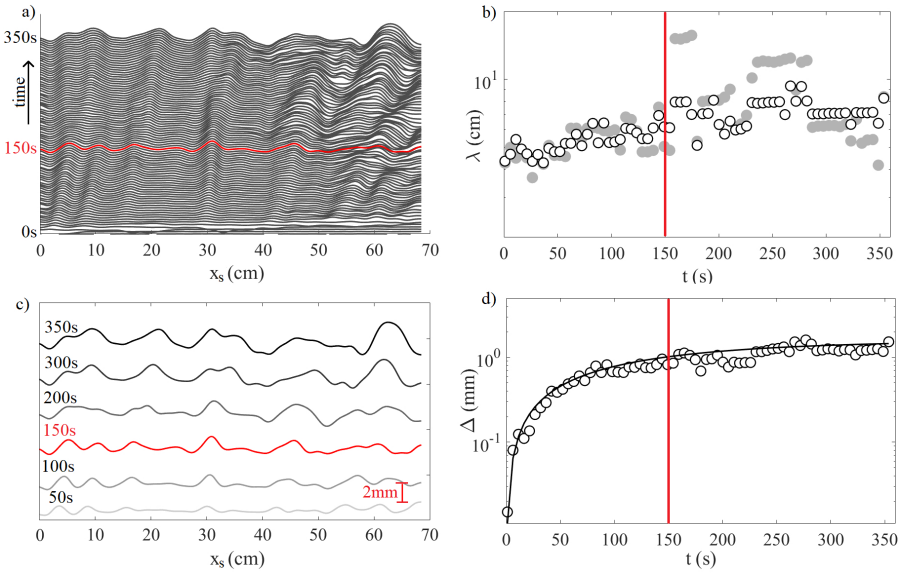

Fig. 11: a) Longitudinal bed profile evolution with time. b) Time evolution of the spatial averaged wavelength λ of the bed forms. c) Longitudinal bed profiles at different times. d) Same as in (b) but for Δ. The vertical red lines indicates the instant $t = 150$s. The gray symbols in b) represent the averaged values for $x_s > 40$cm, while the continuous black line in d) is the theoretical growth of amplitude (Eq. (17)) with $T_S = 150s$.

velocity fields were analyzed, and the results obtained have been compared with those obtained under smooth bottom boundary conditions. The results clearly demonstrate that the presence of the sediment bed induces changes in the dynamics of the dense current. In particular, the vertical velocity component exhibits significant negative oscillations, which can be interpreted as contributions to the incipient motion of sediments. Consequently the shear stress decreases as indicated in Tab.1. The sediment suspension capacity theory developed allows to predict the spatial evolution of sediment concentration in a gravity current up to saturation hence, allows to relate the present results to those obtained by Garcia and Parker (1993)[1]. The distance of maximum concentration (i.e. the suspension capacity), is characterized by the saturation length L_S for which we give an expression in terms of the flow parameters. Of particular interest is Eq. (8) of maximum concentration or carrying capacity that is in good agreement with the correlation given by Celik and Rodi (1991)[17] established for open channel and river flows. Sediment entrainment in a gravity current could result in an increase in buoyancy flux, hence an acceleration of the current with a further increase in carrying capacity. This is not the case here; it would require a much larger scale flow.

Bed forms can be compared with other flow configurations when inner scaling (not Froude numbers) is used, as has been pointed out previously by Ohata

et al. (2023)[33]. The observed bed forms here are ripples, the wavelength of which scales with the Yalin number and Shield stress-particle Reynolds numbers, as proposed by Lapotre et al. (2017)[2]. For ripple amplitude growth we give an expression in terms of a saturation time T_S which is calculated using the theory of Charru et al. (2013)[3]. It is interesting to note that $T_S \approx L_S/u_{*s}$, implying that saturation of sediment concentration and of bed form amplitude are directly related.

The phase speed of the ripples is of the order of 10^{-2} cm/s which is nearly one order of magnitude less than the expected value as cited in [16] for instance.

The slight inclination of the bottom, hence also the sediment bed, notably affects the current by the change of internal $Fr < 1$ to $Fr > 1$, i.e. to Richardson number $Ri < 1$, hence giving rise to KH instabilities. However, the slope (θ=7°) is thought to be negligible. It would be of interest to consider larger slopes as well as large fluxes to determine the slope effect and possible current acceleration on sediment entrainment and bed forms.

Declarations

- Funding. This work is supported by the French National Research Agency in the framework of the "France 2030" program ANR-15-IDEX-0002.
- Conflict of interest. The authors declare that they have no known competing financial interests or personal relationships that could have appeared to influence the work reported in this paper.
- Data availability. Data can be provided upon request.
- Consent for publication. Consent was received from all the authors.
- Author contribution. M.E.N. designed the experiments, M.E.N. and A.M. performed the experiments, M.E.N. processed the raw data to obtain velocity fields. M.R.M and A.M. processed and analyzed the experimental data. E.J.H. developed the theoretical model. All authors discussed and interpreted the results. M.R.M., M.E.N. and E.J.H. wrote the manuscript. All authors reviewed the manuscript.

Appendix A

In order to estimate the concentration of sediment in the water column at each time step, image processing is conducted using the zoomed view to enhance the contrast between the background and particles (see Fig. 5b). The image resolution is designed to detect each particle in the water column, estimating its dimensions and radius to derive a reasonably reliable measure of particle concentration. Considering a camera resolution of $dx = dy = 0.13$ mm for the zoomed view, we selectively considered particles with an area larger than $2dx$ to distinguish them from the PIV particles and filtered particles based on their eccentricity, retaining only those with eccentricity < 0.8, indicative of spherical shapes. The concentration is calculated coarsely as the number of detected particles over a specified reference volume, considering the maximum height of the dense flow and the 5 mm laser layer thickness. We made the

assumption that all particles had a radius of 300 μm and were spherical. The total volume associated with the particles was computed and divided by the reference volume.

References

[1] Garcia, M., Parker, G.: Experiments on the entrainment of sediment into suspension by a dense bottom current. Journal of Geophysical Research: Oceans **98**(C3), 4793–4807 (1993)

[2] Lapotre, M.G., Lamb, M.P., McElroy, B.: What sets the size of current ripples? Geology **45**(3), 243–246 (2017)

[3] Charru, F., Andreotti, B., Claudin, P.: Sand ripples and dunes. Annual Review of Fluid Mechanics **45**, 469–493 (2013)

[4] Charrondière, C., Brun, C., Hopfinger, E.J., Cohard, J.-M., Sicart, J.-E.: Mean flow structure of katabatic winds and turbulent mixing properties. Journal of Fluid Mechanics **941** (2022)

[5] Baringer, M.O., Price, J.F.: Mixing and spreading of the mediterranean outflow. Journal of Physical Oceanography **27**(8), 1654–1677 (1997)

[6] Meiburg, E., Kneller, B.: Turbidity currents and their deposits. Annual Review of Fluid Mechanics **42**, 135–156 (2010)

[7] Hopfinger, E.: Snow avalanche motion and related phenomena. Annual review of fluid mechanics **15**(1), 47–76 (1983)

[8] Rastello, M., Hopfinger, E.J.: Sediment-entraining suspension clouds: a model of powder-snow avalanches. J. Fluid Mech. **509**, 181–206 (2004)

[9] Shi, H., Negretti, M., Chauchat, J., Blanckaert, K., Lemmin, U., Barry, D.A.: Unconfined plunging of a hyperpycnal river plume over a sloping bed and its lateral spreading: Laboratory experiments and numerical modeling. Water Resources Research **58**(8), 2022–032633 (2022)

[10] Altinakar, S., Graf, W.H., Hopfinger, E.J.: Weakly depositing turbidity current on a small slope. J. Hydraul. Res **28**(1), 55–80 (1990)

[11] Pohl, F., Eggenhuisen, J.T., Kane, I.A., Clare, M.A.: Transport and burial of microplastics in deep-marine sediments by turbidity currents. Environmental Science & Technology (2020)

[12] Kostaschuk, R., Nasr-Azadani, M.M., Meiburg, E., Wei, T., Chen, Z., Negretti, M.E., Best, J., Peakall, J., Parsons, D.R.: On the causes of pulsing in continuous turbidity currents. J. Geophys. Res: Earth Surface

123(11), 2827–2843 (2018). https://doi.org/10.1029/2018JF004719

[13] Bründl, M., Bartelt, P., Schweizer, J., Keiler, M., Glade, T.: Review and future challenges in snow avalanche risk analysis. Geomorphological hazards and disaster prevention. Cambridge University Press, Cambridge, 49–61 (2010)

[14] Thorez, S.A., Blanckaert, K., Lemmin, U., Barry, D.A.: From inflow to interflow, through plunging and lofting: uncovering the dominant flow processes of a sediment-rich hyperpycnal river inflow into a stratified lake (2023)

[15] Hickin, E.J.: Hydraulic geometry and channel scour, fraser river, british columbia, canada. In: River Geomorphology, vol. 1995, pp. 155–167 (1995)

[16] Graf, W.H.: Hydraulics of Sediment Transport. McGrawHill, New York (1971)

[17] Celik, I., Rodi, W.: Suspended sediment-transport capacity for open channel flow. Journal of Hydraulic Engineering **117**(2), 191–204 (1991)

[18] Koller, D.K.: Estudo Experimental de Formas de Fundo Geradas Por Correntes de Densidade Salina em Canal de Fundo Móvel

[19] Andreotti, B., Claudin, P.: Aeolian and subaqueous bedforms in shear flows. Philosophical Transactions of the Royal Society A: Mathematical, Physical and Engineering Sciences **371**(2004), 20120364 (2013)

[20] van Rijn, L.C.: Applications of sediment pick-up function. Journal of Hydraulic Engineering **112**(9), 867–874 (1986)

[21] Parker, G., Fukushima, Y., Pantin, H.M.: Self-accelerating turbidity currents. Journal of Fluid Mechanics **171**, 145–181 (1986)

[22] Hu, P., Cao, Z.: Fully coupled mathematical modeling of turbidity currents over erodible bed. Advances in Water Resources **32**(1), 1–15 (2009)

[23] Akiyama, J., Stefan, H.: Turbidity current with erosion and deposition. Journal of Hydraulic Engineering **111**(12), 1473–1496 (1985)

[24] Parker, G., Garcia, M., Fukushima, Y., Yu, W.: Experiments on turbidity currents over an erodible bed. Journal of Hydraulic Research **25**(1), 123–147 (1987)

[25] Conley, D.C., Falchetti, S., Lohmann, I.P., Brocchini, M.: The effects of flow stratification by non-cohesive sediment on transport in high-energy

wave-driven flows. Journal of Fluid Mechanics **610**, 43–67 (2008)

[26] Parker, G., Klingeman, P.C., McLean, D.G.: Bedload and size distribution in paved gravel-bed streams. Journal of the Hydraulics Division **108**(4), 544–571 (1982)

[27] Sequeiros, O.E., Spinewine, B., Beaubouef, R.T., Sun, T., García, M.H., Parker, G.: Characteristics of velocity and excess density profiles of saline underflows and turbidity currents flowing over a mobile bed. Journal of Hydraulic Engineering **136**(7), 412–433 (2010)

[28] Zordan, J., Juez, C., Schleiss, A.J., Franca, M.J.: Entrainment, transport and deposition of sediment by saline gravity currents. Adv. Water Res. **115**, 17–32 (2018)

[29] Kyrousi, F., Leonardi, A., Roman, F., Armenio, V., Zanello, F., Zordan, J., Juez, C., Falcomer, L.: Large eddy simulations of sediment entrainment induced by a lock-exchange gravity current. Adv. Water Res. **114**, 102–118 (2018)

[30] Martin, A., Negretti, M.E., Hopfinger, E.J.: Development of gravity currents on slopes under different interfacial instability conditions. J. Fluid Mech. **880**, 180–208 (2019)

[31] Baas, J.H., Best, J.L., Peakall, J.: Predicting bedforms and primary current stratification in cohesive mixtures of mud and sand. Journal of the Geological Society **173**(1), 12–45 (2016)

[32] Khosronejad, A., Sotiropoulos, F.: Numerical simulation of sand waves in a turbulent open channel flow. Journal of Fluid Mechanics **753**, 150–216 (2014)

[33] Ohata, K., de Cala, I., Dorrell, R.M., Naruse, H., McLelland, S.J., Simmons, S.M., McCaffrey, W.D.: Density stratification controls the bedform phase diagram of saline-gravity currents versus open-channel flows. Sedimentology **70**(4), 1224–1250 (2023)

[34] Negretti, M.E., Flòr, J.B., Hopfinger, E.J.: Development of gravity currents on rapidly changing slopes. Journal of Fluid Mechanics **833**, 70–97 (2017)

[35] Jiménez, J.A., Madsen, O.S.: A simple formula to estimate settling velocity of natural sediments. Journal of waterway, port, coastal, and ocean engineering **129**(2), 70–78 (2003)

[36] Finn, J.R., Li, M.: Regimes of sediment-turbulence interaction and guidelines for simulating the multiphase bottom boundary layer. International

Journal of Multiphase Flow **85**, 278–283 (2016)

[37] Chiew, Y.-M., Parker, G.: Incipient sediment motion on non-horizontal slopes. Journal of Hydraulic Research **32**(5), 649–660 (1994)

[38] Zordan, J., Schleiss, A., Franca, M.J.: Bed shear stress estimation for gravity currents performed in laboratory. Technical report (2016)

[39] Maggi, M.R., Negretti, M.E., Hopfinger, E.J., Adduce, C.: Turbulence characteristics and mixing properties of gravity currents over complex topography. Physics of Fluids **35**(1) (2023)

[40] Turner, J.S.: Buoyancy Effects in Fluids. Cambridge university press, Cambridge (1979)

[41] Flood, R.D., Hiscott, R.N., Aksu, A.E.: Morphology and evolution of an anastomosed channel network where saline underflow enters the black sea. Sedimentology **56**(3), 807–839 (2009)

[42] Hendershot, M.L., Venditti, J.G., Bradley, R.W., Kostaschuk, R.A., Church, M., Allison, M.A.: Response of low-angle dunes to variable flow. Sedimentology **63**(3), 743–760 (2016)

[43] Dorrell, R., Peakall, J., Darby, S., Parsons, D., Johnson, J., Sumner, E., Wynn, R., Özsoy, E., Tezcan, D.: Self-sharpening induces jet-like structure in seafloor gravity currents. Nature communications **10**(1), 1381 (2019)

[44] Duran Vinent, O., Andreotti, B., Claudin, P., Winter, C.: A unified model of ripples and dunes in water and planetary environments. Nature Geoscience **12**(5), 345–350 (2019)